Journal Name

ARTICLE TYPE

Cite this: DOI: 10.1039/xxxxxxxxxx

Propulsion and controlled steering of magnetic nanohelices

Maria Michiko Alcanzare,[1‡] Mikko Karttunen,[2‡] and Tapio Ala-Nissila[3‡]

Received Date
Accepted Date

DOI: 10.1039/xxxxxxxxxx

www.rsc.org/journalname

Externally controlled motion of micro and nanomotors in a fluid environment constitutes a promising tool in biosensing, targeted delivery and environmental remediation. In particular, recent experiments have demonstrated that fuel-free propulsion can be achieved through the application of external magnetic fields on magnetic helically shaped structures. The magnetic interaction between helices and the rotating field induces a torque that rotates and propels them via the coupled rotational-translational motion. Recent works have shown that there exist certain optimal geometries of helical shapes for propulsion. However, experiments show that controlled motion remains a challenge at the nanoscale due to Brownian motion that interferes with the deterministic motion and makes it difficult to achieve controlled steering. In the present work we employ quantitatively accurate simulation methodology to design a setup for which magnetic nanohelices of 30 nm in radius and 180 nm in length (corresponding to previously determined optimal length to radius ratio of 6), with and without cargo, can be accurately propelled and steered in the presence of thermal fluctuations. In particular, we demonstrate fast transport of such nanomotors and devise protocols in manipulating external fields to achieve directionally controlled steering at biologically relevant temperatures.

1 Introduction

The development of artificial nano and micromotors that can be controlled accurately and precisely in spatial and temporal scales has attracted rapidly increasing interest. They are typically catalytically driven [1–13] or magnetically propelled [14–24]. One of the key issues for such nanomotors to be useful for practical purposes is remote motion control and maneuverability. This has been demonstrated where thermal fluctuations are not important such as in the transport, guidance, and release of cells [20–22], single-cell targeted delivery [16] and oil droplet capture [25,26]. Catalytically driven micromotors rely on chemical gradients for self-propulsion, and motion control is made possible through externally manipulated magnetic fields [10–13]. Catalysis-propelled particles require fuel such as hydrogen peroxide, acidic or alkaline solutions which poses a challenge in their biocompatibility for *in vivo* applications [27]. This challenge can be alleviated by creating catalytically driven micromotors that require low concentrations of fuel without compromising their propulsion speeds [28] or using micromotors that propel in biocompatible solutions [29,30]. Magnetic propellers, on the other hand, are suitable candidates for *in vivo* applications since they do not require fuel and most soft biological tissues have very low magnetic susceptibilities [31]. Such propellers have been shown to be driven and elaborately maneuvered, and can perform complex tasks such as cargo fetching and delivery [15,17,18,21]. Their propulsion speeds can be remotely controlled by tuning the field frequencies.

Scaling magnetic propellers down to the nanosize presents a major challenge for controlled motion and maneuverability because of thermal fluctuations [6,13,18,32]; thermal Brownian motion can severely alter the direction of motion and interfere with the propulsion. Schamel *et al.* [18] circumvented the challenge in nanoscale steering by driving the nanopropellers at low frequencies in gels and highly viscous media to damp out thermal fluctuations. In water where biology occurs, however, no propulsion was observed as Brownian effects dominated the propulsion [18].

In our previous work [35], we studied the shape dependence of rotation and propulsion of helically shaped magnetic nanoparticles at constant torque. We found that the maximum propulsion is achieved by balancing competing requirements for rotational stability and minimizing viscous drag. Of various helical shapes,

[1] *HYBER CoE, Department of Applied Physics, Aalto University, FI-00076 Aalto, Finland, maria.alcanzare@aalto.fi*
[2] *Department of Chemistry & Applied Mathematics, Western University, 1151 Richmond Street, London, Ontario, Canada N6A 5B7, mkarttu@uwo.ca*
[3] *QTF CoE, Department of Applied Physics, Aalto University, FI-00076 Aalto, Finland; Centre for Interdisciplinary Mathematical Modelling and Departments of Mathematical Sciences and Physics, Loughborough University, Loughborough, Leicestershire LE11 3TU, UK, tapio.ala-nissila@aalto.fi*
† Electronic Supplementary Information (ESI) available
‡These authors contributed equally to this work

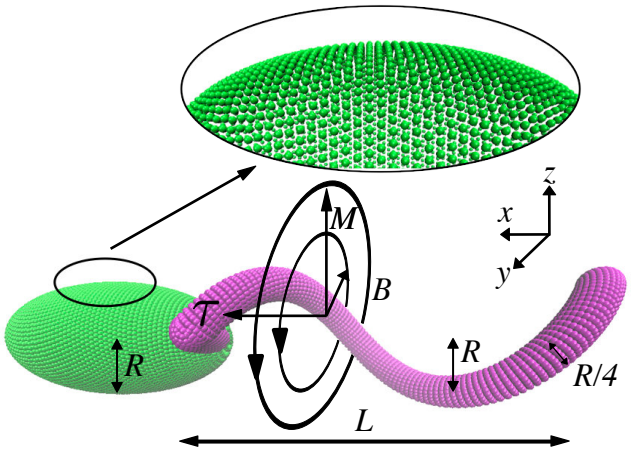

Fig. 1 Node representation of the extended bodies in the fluctuating lattice-Boltzmann - Molecular dynamics method[33]. The optimal helix has $N = 1.25$ turns and a turn length L to radius R ratio of $L/R \approx 6$, with $R = 30$ nm for nanoscale helices. The optional cargo is a prolate spheroid, which minimizes hydrodynamic drag[34] and whose minor axis equals R (See Supporting Information for more details). The magnetic moment of the helix is fixed perpendicular to the long axis such that torque is along the long axis of propulsion, as shown schematically in the figure.

we found that the helix with a circular cross-section and number of turns $N = 1.25$ and length to radius ratio $L/R \approx 6$ exhibits maximal propulsion velocity (cf. Fig. 1, and Figs. 1 and 2 in Ref. 35). Furthermore, for well-defined propulsion and chiral separation in the presence of Brownian motion, the Péclet number must be larger than about 50. In the present work, we extend our previous work[35] to the experimentally relevant case where the helix has a fixed magnetic moment and it is driven by an external magnetic field with varying frequency f. In particular, we show how steered propulsion can be optimized as a function of the magnetic interaction and f. We also consider the case where the helix functions as a cargo-carrying nanomotor, and present a protocol for changing the field for controlled directional steering of the nanopropellers. We use the recently developed fluctuating lattice-Boltzmann method[33,36–39] to quantitatively model the fluid environment and the nanopropellers. Details about the method are provided in Section 2 and Supporting Information (SI).

1.1 Coupled translational and rotational motion by magnetic field

At the scales of micron and less, micro-organisms navigate in water based fluids at very low Reynolds numbers $\mathrm{Re} \ll 1$. They have developed, through billions of years of evolution, helically shaped appendages or flagella with locomotion as the primary function[40]. Artifical micropropellers have a similar shape as the flagella such that as the propeller rotates in the fluid, it pushes the fluid along the direction of its easy axis of propulsion. At low Re, this motion is described by an equation that relates the forces and the torques with the velocity and angular velocity by the generalized resistance tensor:

$$\begin{pmatrix} \mathbf{F} \\ \tau \end{pmatrix} = \begin{pmatrix} \xi^{\mathrm{TT}} & \xi^{\mathrm{TR}} \\ \xi^{\mathrm{RT}} & \xi^{\mathrm{RR}} \end{pmatrix} \begin{pmatrix} \mathbf{v} \\ \omega \end{pmatrix}, \tag{1}$$

where $\mathbf{F}, \tau, \mathbf{v}, \omega$ and $\xi^{\alpha\beta}$ are the applied force, applied torque, translational velocity, angular velocity, and the friction matrix of the particle, respectively[41,42]. Bodies with spherical symmetry have zero non-diagonal elements in their resistance tensor. Screw-shaped bodies have helicoidal symmetry and non-zero off-diagonal terms in Eq. 1. This means that the translational and the rotational motion are coupled *i.e.* rotational motion will result in translational motion and vice versa. Rotation of a magnetic helix can be induced by a torque that is generated by the interaction of its magnetic moment $\mathbf{M}$ with an external magnetic field $\mathbf{B}$. As indicated in Fig. 1, here we set $\mathbf{M}$ to be uniform and perpendicular to the helix's easy axis of rotation. An external field is applied and the torque on the helix is given by $\tau = \mathbf{M} \times \mathbf{B}$ (see Fig. 1). The field frequencies used in the simulations are $f = 10 - 10000$ kHz. The state-of-the-art nanopropeller's magnetic moment, which were driven in highly viscous media, is estimated to be 2×10^{-14} emu[18]. For $MB = (1.5 - 2.5) \times 10^{-18}$ Nm in the simulations and using the experimental value of the magnetic moment, the magnetic field strengths required would be $75 - 125$ mT*. The fastest micropropellers (of 100-150 nm radius) had a propulsion speed of ~ 40 μm/s in water at 150 Hz and 5 mT[14].

2 Computational model

In the limit of $\mathrm{Re} = 0$, the corresponding Stokes equations for particles of arbitrary shapes can be numerically solved and the friction matrix in Eq. 1 unraveled. In our recent work on helical particles we have, however, shown that the Stokes approach is not sufficient for quantitative accuracy in the case of externally driven nanohelices[35]. To this end, we employ the fluctuating lattice-Boltzmann - Molecular Dynamics (LBMD) method of Ref. 33. It incorporates full Navier-Stokes hydrodynamics with consistent thermal fluctuations and a coupling of the fluid to extended MD particles of arbitrary shapes. The fluctuating LBMD has been extensively benchmarked for colloids and polymers[44–46]. The LBMD method is implemented as a package in the open-source molecular dynamics program LAMMPS[38,39]. In the present case, the translational (rotational) Reynolds number for a helix of radius R and length L can be shown[35] to be $\mathrm{Re_T} = \rho v L/\eta$ ($\mathrm{Re_R} = \rho \omega R^2/\eta$), where ρ, v, ω η are the fluid density, propulsion velocity, angular velocity and fluid viscosity, respectively. In the simulations, the typical translational (rotational) Reynolds numbers are about $10^{-4} - 10^{-5}$ ($10^{-4} - 10^{-2}$). Details about the method are provided in the Supporting Information (SI), including the geometry of the cargo, and propulsion velocities and rotational viscous drag without cargo as a function of the number of nodes in Fig. S1.

* Following reference 43, the heating from the magnetic interaction will result in temperature rise of the order of 10^{-2} K per second. Refer to the SI for the details.

3 Results

3.1 Dependence of Propulsion on Frequency

In the limit where Brownian motion can be neglected (Pe $\gg 1$), the total net forces and torques on the helix are due to its magnetic interaction with the external field and the hydrodynamic drag. For propulsion, an external magnetic field of constant amplitude is rotated along a plane with frequency f. The direction of propulsion is perpendicular to the plane of the rotating field (cf. Fig. 1). Both the magnitude of the applied torque and the hydrodynamic drag increase from zero up to $\kappa_{\|} f$ for frequencies that are less than $MB/\kappa_{\|}$, where $\kappa_{\|}$ is the viscous rotational drag coefficient; Fig. S2a shows the response of the hydrodynamic drag on the rotation of the helix. Once the helix has achieved an angular frequency of rotation that is equal to that of the magnetic field, the difference between the applied torque and the magnitude of the hydrodynamic drag goes to zero, and the phase difference between the magnetic moment and the magnetic field becomes constant (Fig. S2b).

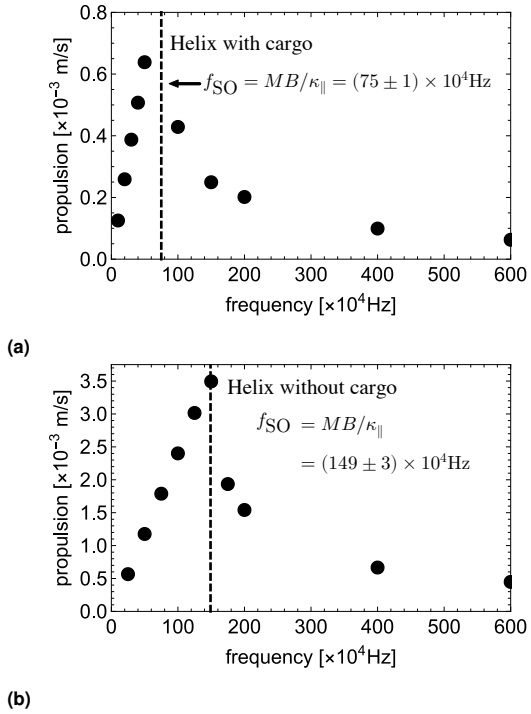

Fig. 2 Propulsion velocities of a helix with a helical diameter of 30 nm driven at $MB = 2.0 \times 10^{-18}$ Nm. The step-out frequencies are indicated by the blue dashed lines. Thermal fluctuations are not included here.

Increasing the frequency of the external field enhances propulsion due to the translational-rotational coupling (Eq. 1), as shown in Fig. 2. The propulsion is linear with the frequency since the torque attains a constant value at steady state. However, when the frequency is greater than a threshold step-out value $f_{SO} = MB/\kappa_{\|}$, the helix eventually lags the magnetic field (Fig. S3). For frequencies less than the step-out frequency, the phase difference reaches a constant value below $\pi/2$ and the resulting external torque also attains a constant value (Fig. S4). For field frequencies greater than the step-out frequency, the phase difference "steps-out" of $\pi/2$ and consequently varies periodically as the process of the magnetic moment lagging the magnetic field and the magnetic field catching up to the magnetic moment repeats itself. Accordingly, the external torque varies periodically for $f > f_{SO}$ as shown in Fig. S4. This is reflected in the strong reduction in propulsion beyond f_{SO} (Fig. 2). We find that the step-out frequency of the helix with an attached cargo (Fig. S4b) is smaller by about a factor of two than the step-out frequency of the helix without the cargo (Fig. S4a). The cargo was chosen to have the shape of a prolate spheroid which minimizes the Stokes drag coefficient[34] and which also has better lipid bilayer penetration than a sphere[47]. This is consistent with the fact that the helix with an attached cargo has a greater viscous drag coefficient due to the additional surface area of the cargo than a helix without an attached cargo (the drag coefficients are given in Table S2.

3.2 Péclet numbers

The importance of Brownian motion to propulsion can be quantified by considering the Péclet number, which is the ratio between the diffusive and the advective time scales. A Péclet number greater than one means that the advective motion dominates over thermal effects. For translational motion, the Péclet number is given by $\mathrm{Pe_T} = vL/D_\mathrm{T}$ and for rotational motion $\mathrm{Pe_R} = \Omega/D_\mathrm{R}$, where D, v and Ω, and L refer to the diffusion coefficient, the propulsion velocity, angular velocity, and length of the helix, respectively[18]. In our previous study we found that nanohelices could be reliably propelled for $\mathrm{Pe_T} \sim 50$[35]. For the 30 nm helices here, the minimum frequencies for $\mathrm{Pe_R} > 1$ are at (1558 ± 5) and (3095 ± 60) Hz with and without cargo, respectively (cf. Table S1). The frequencies used in the simulations thus result in Péclet numbers that are much larger than unity for both with and without cargo as shown in Fig. 3, where we plot the propulsion velocities and the corresponding translational Péclet numbers for two different values of MB with Brownian motion at $T = 300$ K. We note that the highest propulsion speed of the nanohelices that were driven at $MB = 2.0 \times 10^{-18}$ Nm and $f = 149 \times 10^4$ Hz is $\sim 3.5 \times 10^{-3}$ m/s which is ~ 90 times greater than the propulsion of the fastest experimental micropropellers that were driven at 150 Hz ($\sim 40 \times 10^{-6}$ m/s)[14,48].

3.3 Directional steering of nanohelices

In addition to steering propellers along a straight path, directional maneuverability is a crucial aspect for the application of helices as nanomotors and cargo carriers. For the magnetic propellers, reversing the direction of motion is a matter of switching the direction of the rotation of the external magnetic field. Alterations in the direction of motion may be done by changing the direction of the torques or changing the perpendicular plane of the rotating field. Here we demonstrate steering both with and without thermal fluctuations and at high Péclet numbers ($\mathrm{Pe_T} = 370$ and 526 for 700 kHz and 1000 kHz, respectively) such that the external driving is significantly greater than Brownian motion.

Two types of steering were tested corresponding to high and low values of MB. The aim at high MB steering is to avoid the scenario where the magnetic moment of the helix steps out of the

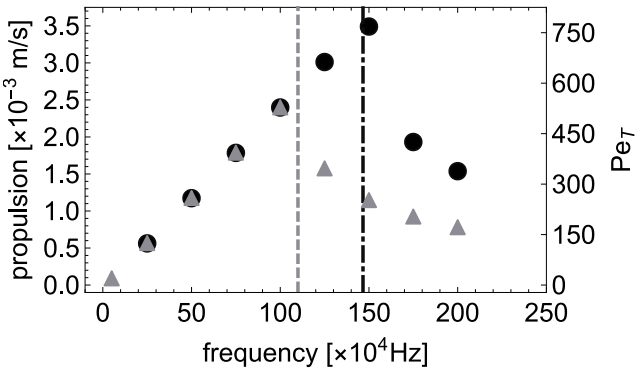

Fig. 3 Propulsion velocity of a helix without an attached cargo with thermal fluctuations at $T = 300$ K. Triangles and circles correspond to a maximum torque of 1.5×10^{-18}Nm and 2.0×10^{-18} Nm, respectively. The dashed lines mark the corresponding step-out frequencies $f_{SO} = (109 \pm 2) \times 10^4$ Hz and $f_{SO} = (149 \pm 3) \times 10^4$ Hz, which increase linearly with MB. The error bars are smaller than the markers (see Figs. S5 and S6). Representative displacement plots at various field frequencies in the presence of thermal fluctuations are shown in Fig. S7.

$\pi/2$ phase with the magnetic field. High MB steering subjects the helix to high external torques during the turn. Low MB turning, on the other hand, results to turns for which the helix steps out of the $\pi/2$ phase for a short time and simultaneously rotates the helix in the opposite direction of the field rotation until it synchronizes back into the rotation of the magnetic field.

Figures 4a-4d demonstrate the case of high MB steering. Two 45° turns were performed at 1000 kHz and $MB = 10 \times 10^{-18}$ Nm. The steering protocol is as follows: first, the nanohelix is propelled for 2.5×10^6 time steps by applying an external torque in the $-x$-direction. Then the direction of the torque is instantaneously changed towards $-(\hat{x} + \hat{y})$ for the same amount of time steps (Fig. S8). In the final part, the helix is propelled in the $-y$-direction. Small oscillations in the displacement along the long axis are present as shown in Figs. 4b and 4c for $0 < t < 0.7 \times 10^{-4}$ s when the helix is propelled along the $-\hat{x}$, and for $1.4 \times 10^{-5} < t < 2.1 \times 10^{-4}$ s when the helix is propelled along $-\hat{y}$. These oscillations in the displacement are not observed in the direction of the propulsion as shown in Fig. 4a and in the transformed coordinates x' rotated by 45° from the x-axis when the helix is turned by 45° at $t = 0.7 \times 10^{-5}$ s (Fig. 4d). These turns were done at high MB such that the magnetic moment of the helix does not step out of the $\pi/2$ phase with the magnetic field. Despite this, the large torque causes the helix to turn with a sudden motion causing a sharp jump in the displacement during the turns (at $t = 0.7 \times 10^{-5}$ s and at $t = 1.4 \times 10^{-5}$ s). These jumps are more prominent in the parametric plot of the trajectory in Fig. 4e where it can also be seen that the intended trajectory is not closely followed by the helix.

In contrast, for low steering at $MB = 1.5 \times 10^{-18}$ Nm with the steering protocol described above, the magnetic moment of the helix momentarily steps out of the $\pi/2$ phase difference. During this stage, it rotates in a direction opposite to the magnetic field until its rotational motion is synchronized with that of the field. This makes controlled directional steering difficult to achieve as demonstrated in Fig. S9 with abrupt, sharp 90° turns.

To overcome this difficulty and to ensure that the helix is kept synchronized with the magnetic field, gradual changes in the direction of the field must be made. To this end, we have devised the following steering protocol. At the beginning the helix is first synchronized with the field (by propelling it for 15 rotations of the magnetic field here). The actual turning begins by fixing the magnetic field in a given direction for a period of time $\delta t = T_1$ to allow the helix to realign with the fixed field as it prepares to be steered. To achieve a turn, the field is then rotated in small increments that add up to θ. After this the field direction is fixed again for $\delta t = T_3$. The time interval for which the gradual changes in the field are done must be $f^{-1} < \delta t < \tau_{\text{relax}}$, where $\tau_{\text{relax}} \approx \delta R^2 / D_T$ is the time scale to traverse a distance of $\delta R \leq L$ by diffusion. In this manner asynchronization is avoided and successful $\theta = 45°$ and $\theta = 90°$ turns are demonstrated for $MB = 1.5 \times 10^{-18}$ Nm in Figs. 4f-4i. Without Brownian motion (blue trajectories in Figs. 4g and 4i) the intended trajectory is faithfully followed due to the lack of sudden jumps. In the presence of thermal fluctuations, the trajectory follows the intended path within the region of diffusive spreading which can be mitigated by optimizing the propulsion velocity. In the simulations we chose $T_1 = 4.4 \times 10^{-6}$ s, $T_2 = 2.9 \times 10^{-6}$ s and $T_2 = 1.5 \times 10^{-6}$ s.

The shaded regions in the parametric plots (Figs. 4g and 4i) represent the regions of diffusional spreading caused by Brownian motion at $T = 300$ K as obtained from the mean square displacement measurements. This inherent spreading, of width δs, that is orthogonal to the direction of propulsion is controlled by the Brownian tracer diffusion coefficient of the helix during the straight segments of the path by $\delta s \approx \sqrt{D_T t_s}$, where t_s is the duration of time from the start of the propulsion. Thus, diffusional spreading can be mitigated by increasing the propulsion velocity (for a given path length), or reducing D_T by lowering the temperature, increasing the propeller size and increasing the viscosity of the fluid[35].

Finally, we demonstrate that smooth turns through curved or circular trajectories with or without thermal fluctuations are also possible as illustrated in Fig. 5. The helix is driven at 700 kHz with $MB = 1.5 \times 10^{-18}$ N m and the perpendicular plane of the rotating magnetic field is rotated by $d\theta = \pi/\delta t'$ for every time step where $\delta t' > f^{-1}$ (in the simulations $\delta t' = 6.28 f^{-1}$). Although the rotation of the perpendicular plane of the magnetic field is along the $\hat{y}$ direction, the resulting path shows a drift in the y direction such that the intended circular path becomes helical. Left and right-handed helices were simulated with different combinations of clockwise and counterclockwise field rotations and directions of steering. In the deterministic simulations, we find that when the helix rotates such that it pushes the fluid inside the circular trajectory, the helix drifts in the opposite direction of the displaced fluid (cf. the diagram in Figs. 5c and 5d)†. In the presence of thermal fluctuations, this drift is totally overcome by Brownian motion since the Péclet number $\text{Pe}_T = 8$ in the z-direction.

† A vector field plot of the fluid velocities can be found in the SI in Fig. S10.

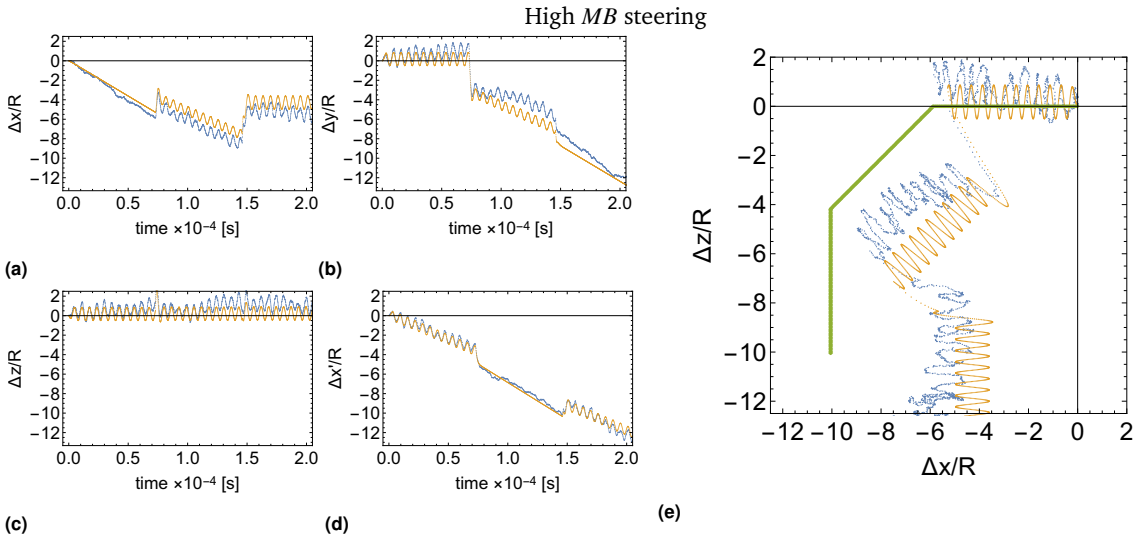

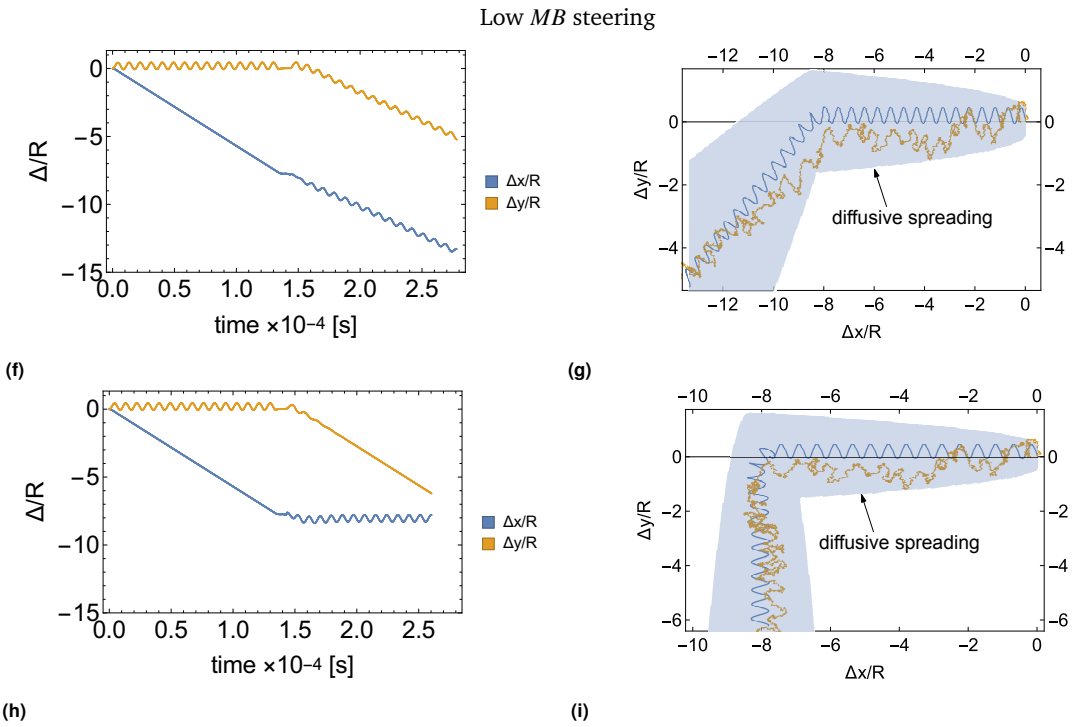

Fig. 4 Figures **(a-e)** illustrate directional high MB steering of a nanohelix at $f = 1000$ kHz with $MB = 10 \times 10^{-18}$ Nm, where the perpendicular plane of the magnetic field is instantaneously changed during the turns. The steering protocol has three stages: propulsion in the x-direction and two consecutive rotations by 45° on the xy plane (see text for details). **(e)** The blue, orange and green trajectories are the paths for steering with thermal fluctuations corresponding to $T = 300$ K, without thermal fluctuations and the intended path, respectively. Panels **(a-c)** are the normalized displacements Δ/R along the normal coordinates, panel **(d)** is the x' displacement in a transformed coordinate that is rotated by 45° in the z-direction, and panel **(e)** is a parametric plot of the trajectory. Due to the jumps, the intended path is not accurately followed. Panels **(f-i)** illustrate low MB steering of a nanohelix at $f = 700$ kHz with $MB = 1.5 \times 10^{-18}$ Nm, where the changes in the magnetic field during the turns are done gradually to prevent asynchronization of the propeller with the field (see text for details). Panels **(f)** and **(h)** show the $\Delta x/R$ and the $\Delta y/R$ displacements for 45° and 90° turns, and panels **(g)** and **(i)** show the corresponding parametric trajectories. The intended path is now faithfully followed. The shaded region indicates diffusive spreading due to Brownian motion at $T = 300$ K.

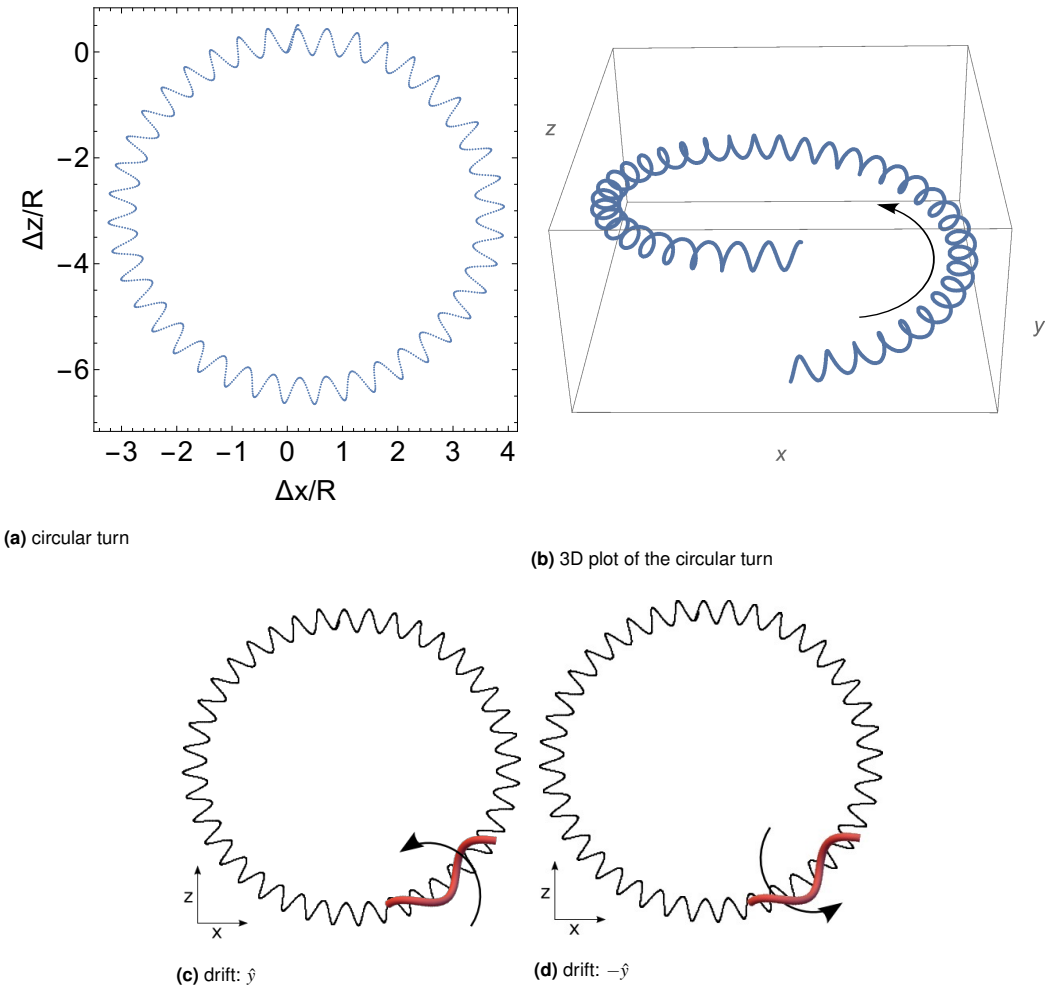

(a) circular turn

(b) 3D plot of the circular turn

(c) drift: $\hat{y}$

(d) drift: $-\hat{y}$

Fig. 5 Panels **(a-b)** show the trajectory of a helix driven at 700 kHz with the perpendicular plane of the field rotated by $d\theta$ in the $\hat{y}$ direction at each time step. The helix drifts in the opposite direction of the displaced fluid the $\hat{y}$ direction. In general, the drift depends on the rotational velocity of the helix as it makes the turn. For angular rotations directed counterclockwise to the circular trajectory (panel **(c)**) the helix drifts in the $+\hat{y}$ direction, while for clockwise rotations the helix drifts in the $-\hat{y}$ direction (panel **(d)**).

4 Summary and conclusions

In conclusion, we have shown that nanoscale helical propellers can be used for controlled motion and steering at high Péclet numbers. The propulsion velocities and Pe of the propellers can be conveniently adjusted through the magnetic field frequencies for frequencies that are less than the step-out value, which can be determined from the ratio of the magnetic interaction to drag as $f_{SO} = MB/\kappa_{\|}$. Extending the range for higher propulsion velocities is possible by increasing both the field frequency and MB or reducing drag. Compared with the fastest artificial controllable chiral micropropellers of ~ 150 nm in size, which have a maximum propulsion speed of ~ 40 μm/s at 150 Hz[14,48], our results show that nanoscale propellers of ~ 30 nm in radius and 180 nm in length can be propelled up to $\sim 10^{-3}$ m/s at $100 \sim$ kHz with full control. With these propulsion speeds, it is possible to attain $\mathrm{Pe_T} > 100$, allowing spatial and temporal control of the motion *in the presence of thermal fluctuations*.

As far as we know, up to date no experimental system has reached or probed the frequency range or the field strengths used here. Field values are close, though. Typical field strengths used in experiments are < 10 mT. In our work, we used torques in the range of $MB = (1.5 - 2.0) \times 10^{-18}$ Nm which corresponds to magnetic fields of $75 - 125$ mT. Schamel and co-workers[18] used field strengths up to 10 mT and Peters *et al.*[49] applied fields of 30 mT in their studies of micron size magnetic helices. As for frequencies, they are commonly in the range of tens of Herz, the highest ones being hundreds of Hz[14,50,51]. Whether or not experiments can get to the kHz domain remains to be seen but it cannot be categorically ruled out. Our work shows that such high frequencies are in fact necessary to provide controlled propulsion in water for submicron (< 200 nm) helices. A recent general review of nano- and microswimmers has been provided by Nain and Sharma[52] while Chen *et al.* focus on magnetically driven systems[53].

When comparing with experiments there is an additional issue. In our previous article[35], we discussed structural optimization of helical particles. In particular: a) we found that helix (as op-

posite to a helicoid) is the optimal shape, b) the optimal length to radius (L/R) ratio is about 6, and c) the maximum velocity is achieved with $L/R \approx 6$ and the number of helical turns being 1.25. All of these were applied in the current study. Using optimal parameters makes a significant difference in helices' speeds; when the number of helical turns increases from the optimum, velocity drops significantly (close to a factor of 2 when the number of helical turns is doubled from the optimal 1.25) due to increased drag (see Fig. 2b in Ref. 35). Most experimental systems have significantly more turns than the optimum 1.25. Increasing size increases drag and improves the stability of the motion.

Conflicts of interest

There are no conflicts to declare.

Acknowledgements

This work was supported in part by the Academy of Finland through its Centres of Excellence Programme (2012-2017) under Project No. 251748 and Aalto Energy Efficiency Research Programme. We acknowledge the computational resources provided by Aalto Science-IT project and CSC-IT. MK would acknowledges the financial support of Natural Sciences and Engineering Research Council of Canada Discovery and Canada Research Programs. The graphical representations in the Fig. 1 were rendered using VMD[54].

Notes and references

1 W. F. Paxton, K. C. Kistler, C. C. Olmeda, A. Sen, S. K. St. Angelo, Y. Cao, T. E. Mallouk, P. E. Lammert and V. H. Crespi, *J. Am. Chem. Soc.*, 2004, **126**, 13424–13431.

2 W. F. Paxton, A. Sen and T. E. Mallouk, *Chem.–Eur. J.*, 2005, **11**, 6462–6470.

3 Y. Wang, R. M. Hernandez, D. J. Bartlett, J. M. Bingham, T. R. Kline, A. Sen and T. E. Mallouk, *Langmuir*, 2006, **22**, 10451–10456.

4 R. Laocharoensuk, J. Burdick and J. Wang, *ACS Nano*, 2008, **2**, 1069–1075.

5 H. Ke, S. Ye, R. L. Carroll and K. Showalter, *J. Phys. Chem. A*, 2010, **114**, 5462–5467.

6 T. Mirkovic, N. S. Zacharia, G. D. Scholes and G. A. Ozin, *Small*, 2010, **6**, 159–167.

7 A. A. Solovev, W. Xi, D. H. Gracias, S. M. Harazim, C. Deneke, S. Sanchez and O. G. Schmidt, *ACS Nano*, 2012, **6**, 1751–1756.

8 X. Ma, K. Hahn and S. Sanchez, *J. Am. Chem. Soc*, 2015, **137**, 4976–4979.

9 M. Safdar, O. M. Wani and J. Jänis, *ACS Appl. Mater. Interfaces*, 2015, **7**, 25580–25585.

10 T. R. Kline, W. F. Paxton, T. E. Mallouk and A. Sen, *Angewandte Chemie International Edition*, 2005, **44**, 744–746.

11 J. Burdick, R. Laocharoensuk, P. M. Wheat, J. D. Posner and J. Wang, *J. Am. Chem. Soc*, 2008, **130**, 8164–8165.

12 D. Kagan, R. Laocharoensuk, M. Zimmerman, C. Clawson, S. Balasubramanian, D. Kang, D. Bishop, S. Sattayasamitsathit, L. Zhang and J. Wang, *Small*, 2010, **6**, 2741–2747.

13 J. Wang and K. M. Manesh, *Small*, 2010, **6**, 338–345.

14 A. Ghosh and P. Fischer, *Nano Lett.*, 2009, **9**, 2243–2245.

15 S. Tottori *et al.*, *Adv. Mater.*, 2012, **24**, 811–816.

16 R. Mhanna, F. Qiu, L. Zhang, Y. Ding, K. Sugihara, M. Zenobi-Wong and B. J. Nelson, *Small*, 2014, **10**, 1953–1957.

17 W. Gao, D. Kagan, O. S. Pak, C. Clawson, S. Campuzano, E. Chuluun-Erdene, E. Shipton, E. E. Fullerton, L. Zhang, E. Lauga and J. Wang, *Small*, 2012, **8**, 460–467.

18 D. Schamel, A. G. Mark, J. G. Gibbs, C. Miksch, K. I. Morozov, A. M. Leshansky and P. Fischer, *ACS Nano*, 2014, **8**, 8794–8801.

19 D. Walker, M. Kübler, K. I. Morozov, P. Fischer and A. M. Leshansky, *Nano Lett.*, 2015, **15**, 4412–4416.

20 S. Sanchez, A. A. Solovev, S. Schulze and O. G. Schmidt, *Chem. Commun.*, 2011, **47**, 698–700.

21 M. Medina-Sánchez, L. Schwarz, A. K. Meyer, F. Hebenstreit and O. G. Schmidt, *Nano Lett.*, 2016, **16**, 555–561.

22 V. Magdanz, M. Guix, F. Hebenstreit and O. G. Schmidt, *Adv. Mater.*, 2016, **28**, 4084–4089.

23 C. Bechinger, R. Di Leonardo, H. Löwen, C. Reichhardt, G. Volpe and G. Volpe, *Rev. Mod. Phys*, 2016, **88**, 045006.

24 R. Dreyfus, J. Baudry, M. L. Roper, M. Fermigier, H. A. Stone and J. Bibette, *Nature*, 2005, **437**, 862–865.

25 G. Zhao, T. H. Seah and M. Pumera, *Chem. Eur. J.*, 2011, **17**, 12020–12026.

26 M. Guix, J. Orozco, M. Garciá, W. Gao, S. Sattayasamitsathit, A. Merkoçi, A. Escarpa and J. Wang, *ACS Nano*, 2012, **6**, 4445–4451.

27 H. Wang, G. Zhao and M. Pumera, *J. Am. Chem. Soc.*, 2014, **136**, 2719–2722.

28 W. Gao, S. Sattayasamitsathit, J. Orozco and J. Wang, *J. Am. Chem. Soc.*, 2011, **133**, 11862–11864.

29 W. Gao, A. Pei and J. Wang, *ACS Nano*, 2012, **6**, 8432–8438.

30 F. Mou, C. Chen, H. Ma, Y. Yin, Q. Wu and J. Guan, *Angew. Chem. Int. Ed.*, 2013, **52**, 7208–7212.

31 J. F. Schenck, *Med. Phys.*, 1996, **23**, 815–850.

32 A. Ghosh, D. Paria, G. Rangarajan and A. Ghosh, *The journal of physical chemistry letters*, 2014, **5**, 62–68.

33 S. T. T. Ollila, C. Denniston, M. Karttunen and T. Ala-Nissila, *J. Chem. Phys.*, 2011, **134**, 064902.

34 M. Zabarankin and A. Molyboha, *SIAM J. Appl. Math.*, 2010, **70**, 1788–1809.

35 M. M. Alcanzare, V. Thakore, S. T. T. Ollila, M. Karttunen and T. Ala-Nissila, *Soft Matter*, 2017, **13**, 2148–2154.

36 S. T. T. Ollila, C. Smith, T. Ala-Nissila and C. Denniston, *Multiscale Model. Sim.*, 2013, **11**, 213–243.

37 F. Mackay and C. Denniston, *J. Comput. Phys.*, 2013, **237**, 289–298.

38 F. Mackay, S. Ollila and C. Denniston, *Comput. Phys. Commun.*, 2013, **184**, 2021–2031.

39 S. Plimpton, *J. Comput. Phys.*, 1995, **117**, 1–19.

40 K. F. Jarrell and M. J. McBride, *Nat Rev Micro*, 2008, **6**, 466–476.

41 E. M. Purcell, *Am. J. Phys*, 1977, **45**, 3–11.
42 E. Lauga and T. R. Powers, *Rep. Prog. Phys.*, 2009, **72**, 096601.
43 A. E. Deatsch and B. A. Evans, *Journal of Magnetism and Magnetic Materials*, 2014, **354**, 163–172.
44 S. T. Ollila, C. Denniston, M. Karttunen and T. Ala-Nissila, *Soft Matter*, 2013, **9**, 3478–3487.
45 S. T. Ollila, C. Denniston, M. Karttunen and T. Ala-Nissila, *Phys. Rev. Lett.*, 2014, **112**, 118301.
46 F. E. Mackay, K. Pastor, M. Karttunen and C. Denniston, *Soft Matter*, 2014, **10**, 8724–8730.
47 K. Yang and Y.-Q. Ma, *Nature Nanotechnology*, 2010, **5**, 579.
48 O. S. Pak, W. Gao, J. Wang and E. Lauga, *Soft Matter*, 2011, **7**, 8169–8181.
49 C. Peters, O. Ergeneman, P. D. W. García, M. Müller, S. Pané, B. J. Nelson and C. Hierold, *Adv. Func. Mat.*, 2014, **24**, 5169–5169.
50 J. Li, T. Li, T. Xu, M. Kiristi, W. Liu, Z. Wu and J. Wang, *Nano Lett.*, 2015, **15**, 4814–4821.
51 D. Gong, J. Cai, N. Celi, L. Feng, Y. Jiang and D. Zhang, *J. Magn. Magn. Mat.*, 2018, **468**, 148–154.
52 S. Nain and N. Sharma, *Frontiers Life Sci.*, 2014, **8**, 2–17.
53 X.-Z. Chen, M. Hoop, F. Mushtaq, E. Siringil, C. Hu, B. J. Nelson and S. Pané, *App. Mat. Today*, 2017, **9**, 37–48.
54 W. Humphrey, A. Dalke and K. Schulten, *J. Mol. Graphics*, 1996, **14**, 33–38.